ChemPubSoc Europe

DOI: 10.1002/cphc.201402405

CHEMPHYSCHEM Articles

Fluorescence Confocal Polarizing Microscopy of a Fluorescent Bent-Core Liquid Crystal Exhibiting Polarization Splay Modulated (B7) Structures and Defects

Rajdeep Deb,[a, b] Matt Oneill,[a] Nandiraju. V. S. Rao,[b] Noel A. Clark,*[a, c] and Ivan I. Smalyukh*[a, c, d, e]

The B7 phases of bent-core molecules are polarization splay modulated fluid smectics that exhibit an unusually complex variety of exotic macroscopic structures, textures, and defects visible in polarized light microscopy. Herein we describe optical studies of these structures using fluorescence confocal polarizing microscopy (FCPM) and depolarized transmission optical microscopy to probe their organization in three dimensions. These experiments utilize recently reported fluorescent bent-core molecules designed to give strong polarized fluorescence. This new bent-core molecular family provides the means for probing a variety of bent-core phases and structures by using FCPM and multiphoton fluorescence nonlinear imaging techniques. Comparative textural analysis of the B7 structures obtained using different types of imaging and the corresponding structural models are discussed.

1. Introduction

The study of the structure of the polarization splay modulated (PSM) (B7) phases of bent-core molecules has evoked great interest in recent years. This is because of their striking textures and defects observable in polarized light microscopy,[1–8] and because of the discovery of polarization splay modulation and the resulting layer undulation, which serves as a basis for understanding the exotic macroscopic behavior of these molecules.[9] Many compounds possessing such phases have been reported, mostly five-ring materials of molecules built around a central 1,3-phenyl ring.[10–12]

[a] Dr. R. Deb,[+] M. Oneill,[++] Prof. N. A. Clark, Prof. I. I. Smalyukh
Department of Physics & Liquid Crystal Materials Research Center
University of Colorado, Boulder, CO 80309 (USA)
E-mail: noel.clark@colorado.edu

[b] Dr. R. Deb,[+] Prof. N. V. S. Rao
Department of Chemistry, Assam University
Silchar 788011 (India)

[c] Prof. N. A. Clark, Prof. I. I. Smalyukh
Materials Science and Engineering Program
University of Colorado, Boulder, CO 80309 (USA)
E-mail: ivan.smalyukh@colorado.edu

[d] Prof. I. I. Smalyukh
Department of Electrical, Computer and Energy Engineering
University of Colorado, Boulder, CO 80309 (USA)

[e] Prof. I. I. Smalyukh
Renewable and Sustainable Energy Institute
National Renewable Energy Laboratory
University of Colorado, Boulder, CO 80309 (USA)

[+] Current address:
JRE Group of Institutions
UP 201308 (India)

[++] Current address:
Miyota Development Center America
Longmont CO 80503 (USA)

Recently, we reported the structure and phase behavior of two series of asymmetric as well as isomeric four-ring bent-core mesogens with an ester linkage at the molecular bend.[13] From the molecular architectural point of view, these materials deviate not only from the usual linear molecular architecture of liquid crystals (LCs), but are also quite different from the conventional bent-core molecules derived from the 1,3-phenyl ring,[14–16] or those based on the "hockey-stick" molecular architecture.[17–19] The molecules reported here are able to form smectic LC phases with spontaneously chiral and polar layers (SmCP phases); including the PSM (B7) variants. Thus, interesting comparisons of mesophase morphology could be made with the B7 phases formed by the conventional banana molecules. Additionally, and of key importance for the study reported here, these compounds were designed to exhibit strong photoluminescence, the first family of SmCP phases to do so. Photophysical characterization showed fluorescent emission in the green region from all the homologous compounds reported here.

The structures exhibited by the PSM phase have attracted the application of a variety of imaging techniques to investigate their characteristics, including freeze fracture transmission electron microscopy (FFTEM), atomic force microscopy (AFM) and transmission and reflection optical microscopy (TOM and ROM).[20] In the past, the fluorescence confocal polarizing microscopy (FCPM) technique has been used on non-bent-core LCs to visualize the distribution of fluorescent dye, providing insight into the spatial orientational distribution of different dye-tagged LC systems.[21–23] Herein we use FCPM to probe molecular orientational distributions in B7 textures by tailoring and fine tuning the intrinsic light generating capabilities of these newly synthesized bent-core compounds. Textural analysis of the B7 phase structures in light of the FCPM and depo-

larized transmission optical microscopy (DTOM) imaging techniques is presented and the corresponding structural models are discussed.

In addition to adding another powerful imaging tool for exploring the complex textures of the bent-core phases, the present work extends the science of bent-core LCs in two other important ways. Firstly, by obtaining the principal bent-core phases with molecules having only four rings, this work expands the range of molecular structures useful for bent-core design. Secondly, obtaining the principal bent-core phases with molecules that are strongly fluorescent promises a variety of optical probes of molecular organization in three-dimensions (3D)[24,25] and applications for bent-core systems including, for example, lasing.

1.1. The B7 Phase

The hierarchy of structure in a B7 texture is shown schematically in Figure 1. It begins in Figure 1 a with the spontaneous fluid smectic layering of bent core molecules with long axes tilted away from the normal layer, and long range polar ordering red arrows, as found in the B2 phases.[15] The handedness of the B2 structure is left (outside molecules) or right (centre molecules), depending on the molecular tilt direction. However, the B2 state of uniform inlayer polar ordering is inherently unstable as the local preference of the polarization field is to be splayed, as shown, principally because of the details of the steric packing of the molecules. However, the layer plane cannot be filled by uniform splay, but splay can be accommodated in nonspatially homogeneous structures such as the splay stripe domains sketched in Figure 1 a. In the boundary surfaces of the defects between neighboring stripes (bold vertical lines) the molecules are less tilted and therefore the layers are thicker, producing the distinctive layer undulation that is characteristic of the B7 phase.[9] There are many variations of this periodic layer undulation, depending on the relative orientation of the polarization direction (parallel or antiparallel), relative handedness in neighboring stripes, and degree of relative layer displacements at the defect lines, with half layer displacement leading to the B1 phases. The combination of the periodicities of the splay stripe/undulations and the smectic layering forms a two dimensional lattice in the bulk 3D phase, as sketched in the example of Figure 1 a, a structure having the symmetry of a LC columnar phase.

This undulated B2 smectic grows from the isotropic phase through a first order transition, characterized by distinct interfaces between the two phases. The smectic layering exhibits a strong preference to be locally parallel to the phase boundary interfacial plane.[9] This leads on the micron-length scale to the dominant structural feature of the B7 textures, the linear filaments of closed nested cylinders sketched in Figure 1 b. This basic motif produces the growth of the long filament structures observed as the B7 grows in from the isotropic, and, in particular, their translational symmetry, stabilized by the smectic layer and undulation lattices.[9] It was also proposed that such filaments were responsible for the beautiful conformal domain textures of the B7, as sketched in Figure 1 c.

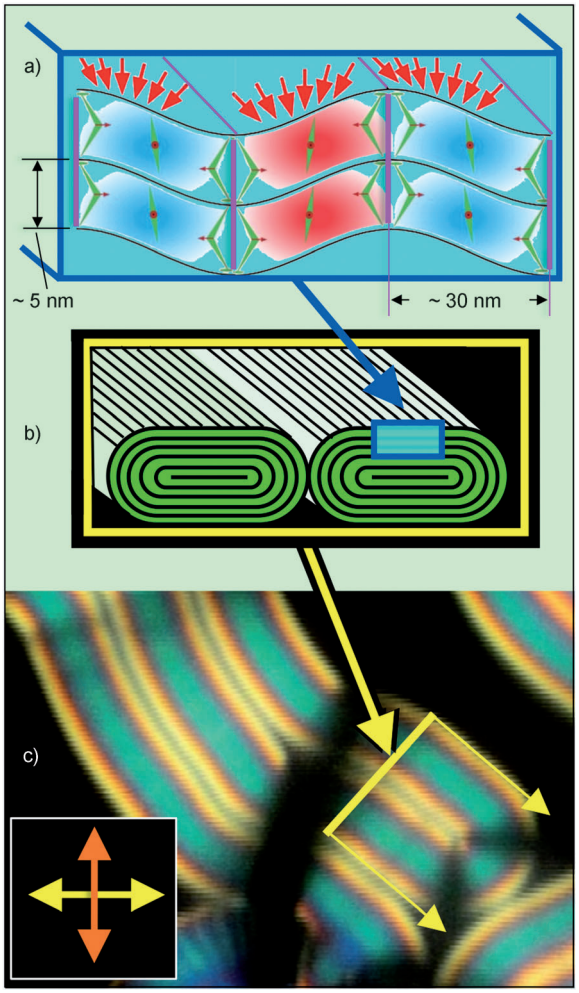

Figure 1. a) B7 structure showing local tilted polar chiral (B2-like) fluid smectic layers which are unstable against spontaneous polarization splay. Splay appears in the form of stripe domains which, in turn, produce periodic layer undulations. The resulting 2D lattice forms a fluid LC with columnar symmetry. b) The preference for the B7 smectic layers to be parallel to the isotropic interface stabilizes B7 filaments of nested smectic layers, represented in this paper as racetracks. c) B7 texture illustrating the relation between the B7 filaments and the conformal domains in (b).

These filaments flattened between glass plates and can bend and fold in on themselves but maintain a fixed local structure, again stabilized by the 2D lattice.[9] The experiments presented here, which enable the first three dimensional view of the B7 textures, confirm this view and reveal the wide variety of structures that the B7 filaments can adopt.

Experimental Section

Methods

For FCPM studies with the excitation beam of $\lambda = 488$ nm, Ar-ion laser was introduced into an inverted microscope (IX-81, Olympus) and focused tightly into a sample by a dry objective (10X, N A = 0.3) into a small voxel (volume pixel, $\approx 1\ \mu m^3$) in the cell.[26] The fluorescent light from this volume was detected by a photomultiplier tube in the spectral region of $\lambda = 510$–550 nm selected by interference filters. The signal arising from the neighboring region of the

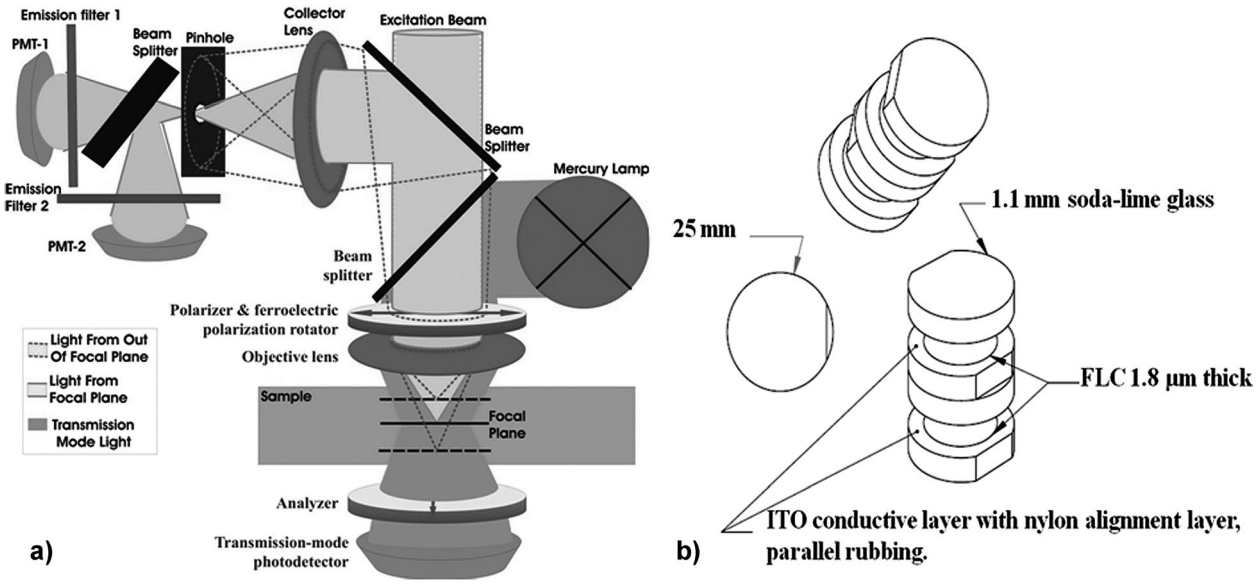

Figure 2. a) Schematic of integrated FCPM and DTOM setup, PMT is a photomultiplier tube and b) diagrammatic representation of the cell used for controlled polarized excitation.

voxel was prevented from reaching the detector by having a pinhole in the detection image plane (Figure 2a). The inspected voxel and the pinhole were confocal, so that only the light coming from the probed voxel reached the detector. This enabled diffraction-limited imaging resolution, not only in the lateral plane, but also along the optical axis of the microscope. In addition to fluorescence polarizing confocal microscopy, this setup allowed us to perform DTOM studies using the light of a scanned excitation laser beam transmitted through the sample. A 3D image of the sample was typically obtained by using a tightly focused laser beam that raster-scans the lateral plane (perpendicular to the microscope optical axis) of the sample. Then, by moving the computer controlled nano-positioning sample-stage step-wise along the axial direction, the scan was repeated at each axial depth. As a result, a stack of submicron horizontal optical slices was obtained and stored in the computer memory, which was then further software-processed to reconstruct a fluorescence 3D image of the orientational pattern of the molecular alignment. The controlled polarized excitation during imaging with FCPM was achieved by introducing the polarization rotator before the objective lens, which enabled controlled polarized excitation. The schematic representation of the polarization rotator is shown in Figure 2b and a brief description of its fabrication and operation is detailed below.

To obtain the ferroelectric polarization rotator for the control of the linear polarization of laser excitation light, two 25×25 mm transmissive cells were prepared with a 1.8 μm cell gap in a class 100 clean room environment. For the cell thickness control, monodisperse 1.8 μm spacer balls were incorporated into the perimeter glue as well as dispersed across the cell field. Cells were constructed of 1.1 mm thick soda-lime glass coated with indium tin oxide and a nylon alignment layer with manual parallel buffing. The buffing cloth was a typical rayon-cloth. Norland 68 optical adhesive was used for both cell construction and lamination of the cells. After construction cells were filled with FLC mixture MX8068 (obtained from Miyota Development Center America), the standard material for photonics products. The cells were inspected for alignment defects as well as to ensure that contrast ratio was at least 1000:1 and optical rise time was <50 μs. Cells were laminated together to provide phase retardations that yielded linear polarizations of the outgoing excitation light at $\theta=0$, 45, and 90 degrees with respect to the initial polarization of the incident $\lambda=488$ nm Ar laser light as well as circularly polarized laser light. To provide the above retardations the cells were wired to a ±3.0 V DC power supply; the electric field across each individual cell from the stack was controlled independently using a three way switch selecting the applied voltage to be $+3$, -3, or 0 V. The ability of fast switching between different linear and circular polarizations of the laser excitation light was critical from the standpoint of view of analyzing 3D structures of molecular organizations in the studied system.

Molecular Design Considerations

An important goal in extending the applicability of 3D imaging with FCPM into different liquid crystalline systems is to incorporate the ability to yield strong fluorescence into the molecules making the LC. This avoids the principal limitations of using dye-doping, including limited solubility of fluorescent dyes in LC hosts, and alteration of the LC properties by the doping. Here we introduced fluorescence into characteristic banana phases, opening the way to take advantage of their promising photophysical properties for device applications.[27–29] The result was achieved by the judicious choice of the bent central core and the substituents, including an appropriate structure with intramolecular H-bonding, which is not only intrinsically fluorescent but also exhibits the fluid smectic PSM (B7) phase.

Materials

The synthesis of B7-forming fluorescent materials was relatively straightforward, but nevertheless involved some interesting chemistry in the purification step. Sequential use of an esterification reaction and Schiff's base condensation was used to obtain the final product (Scheme 1). The compounds under investigation belong to a new class of bent-core mesogens in which the central fragment consists of two nonlinearly substituted benzene rings, connected through a flexible ester linkage. The condensation of 4-*n*-alkyloxy salicylaldehyde with 3-amino phenyl-4-aminobenzoate

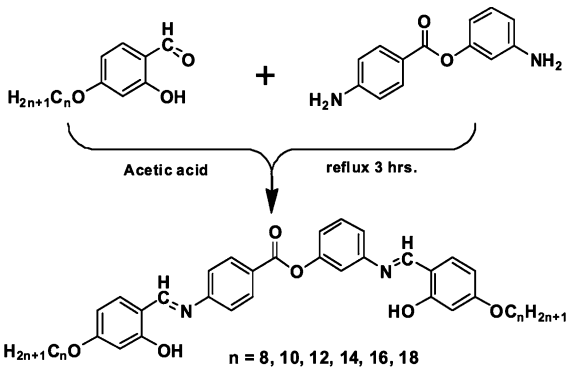

Scheme 1. Synthesis of the compounds **34-*n*OH**, $n = 8$, 10, 12, 14, 16, 18.

in presence of a few drops of glacial acetic acid yielded the target bent shaped compounds [3-(*N*-4′-*n*-alkyloxysalicylidene)-aminophenyl]-[4-(*N*-4′-*n*-alkyloxysalicylideneamino)-benzoate (**34-*n*OH**) (Scheme 1). To avoid the formation of side products under cold conditions in the solution, the precipitated compounds were filtered when the solution was hot to yield the pure compounds. The compounds were further recrystallized repeatedly to get the pure samples. The formation of all the compounds was confirmed by ^{1}H NMR and IR spectroscopy and the purity was established by elemental analysis.[13]

2. Results and Discussion

2.1. Mesomorphic Properties

The transition temperatures, enthalpies and entropies associated with the phase transitions of all the compounds of the homologous series **34-*n*OH** ($n = 8$, 10, 12, 14, 16, 18) are presented in Table 1. These are shown as a function of the number of carbon atoms in the terminal alkyl chains obtained from DSC at a scan rate of 10 °C min^{-1} in the first heating and cooling scans. The textures of the mesophases of all synthesized bent-core compounds (**34-*n*OH**) are quite similar. The phase transition temperatures as a function of the number of carbons in the end alkyl chain length is depicted in Figure 3.

The compound with carbon atoms $n = 10$ in the alkyl chain length had a larger mesophase thermal range. All the compounds were found to exhibit only one mesophase, having the B7 type texture. The mesophase assignments made by DTOM were confirmed by X-ray diffraction (XRD) analysis. The analysis of the powder XRD patterns of the liquid crystalline phases of the representative compound **34-*14*OH**, obtained on a diffractometer with $\delta q = 0.0005$ Å^{-1} resolution at the National Synchrotron Light Source, revealed a phase exhibiting a multi-peak structure near the principal (001) lamellar reflection. This kind of pattern is commonly observed for the B7 phase,[9] thereby confirming the identification of the liquid crystalline phase of **34-*14*OH** to be B7.[13]

The observed optical textures exhibited by a representative compound, **34-*14*OH** are presented in Figure 4. DSC supports the phase-transition temperatures determined by optical polarizing microscopy. Upon the very slow cooling of the isotropic liquid, the mesophase defect textures exhibited by **34-*14*OH**, as shown in (Figure 4a), revealed the co-existence of different

Table 1. Mesophases, transition temperatures [°C], associated enthalpy [kJ mol^{-1}], and entropy [J mol^{-1} K^{-1}] values [in square brackets] of the compounds **34-*n*OH**.

Compound	R	Cr	Heating Cooling	B7	Heating Cooling	I
34-*8*OH	C_8H_{17}	●	–	●	114.8 [*37.5, 96.8*]	●
		●	100.5 [*10.3, 27.6*]	●	107.0 [*10.4, 27.5*]	●
34-*10*OH	$C_{10}H_{21}$	●	111.2 [*26.9, 69.9*]	●	113.5 [*2.3, 5.9*]	●
		●	90.2 [*32.4, 89.4*]	●	111.3 [*11.4, 29.7*]	●
34-*12*OH	$C_{12}H_{25}$	●	108.8 [*21.0, 55.1*]	●	114.9 [*3.2, 8.0*]	●
		●	92.4 [*35.0, 96.0*]	●	113.4 [*4.8, 12.6*]	●
34-*14*OH	$C_{14}H_{29}$	●	110.6 [*50.2, 131.0*]	●	116.0 [*16.6, 42.8*]	●
		●	99.0 [*57.4, 154.3*]	●	114.4 [*16.8, 43.3*]	●
34-*16*OH	$C_{16}H_{33}$	●	112.9 [*41.7, 108.1*]	●	115.0 [*4.2, 10.84*]	●
		●	103.6 [*59.2, 157.3*]	●	113.6 [*9.9, 25.6*]	●
34-*18*OH	$C_{18}H_{37}$	●	104.8 [*22.8, 60.4*]	●	108.5 [*5.3, 14.0*]	●
		●	–	●	101.8 [*64.2, 171.3*]	●

All the reported temperatures are the peak recorded in DSC thermographs in the first heating and cooling cycles at the heating and cooling rates of 10 °C min^{-1}. Additional crystal to crystal transitions have been observed in the **34-*n*OH** series of compounds.

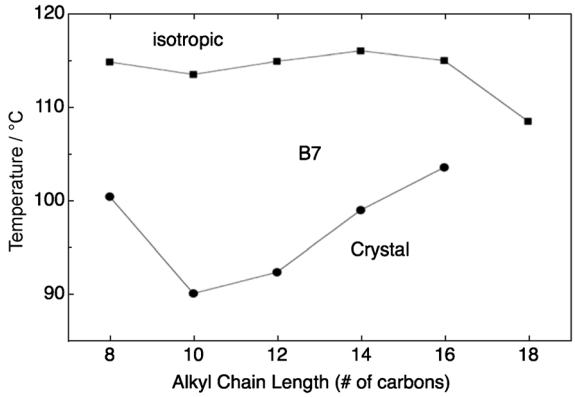

Figure 3. Phase transition temperatures as a function of the number of carbons in the alkyl chain length for the **34-*n*OH** series.

types of long spiral colorful helical ribbons (beaded-, screw-like). Some of these ribbons show the remarkable constancy of the pitch all along the length and the stability of these spiral features depends on the thickness of the sample.

The other remarkable feature of these compounds is the spectacular display of focal conic-like conformal domains (Figure 4b) modulated with stripes and checkerboard patterns. A peculiarity that attracts particular attention is the formation of checkerboard patterns out of the conformal domain with a fan-shaped texture having extinction brushes parallel and

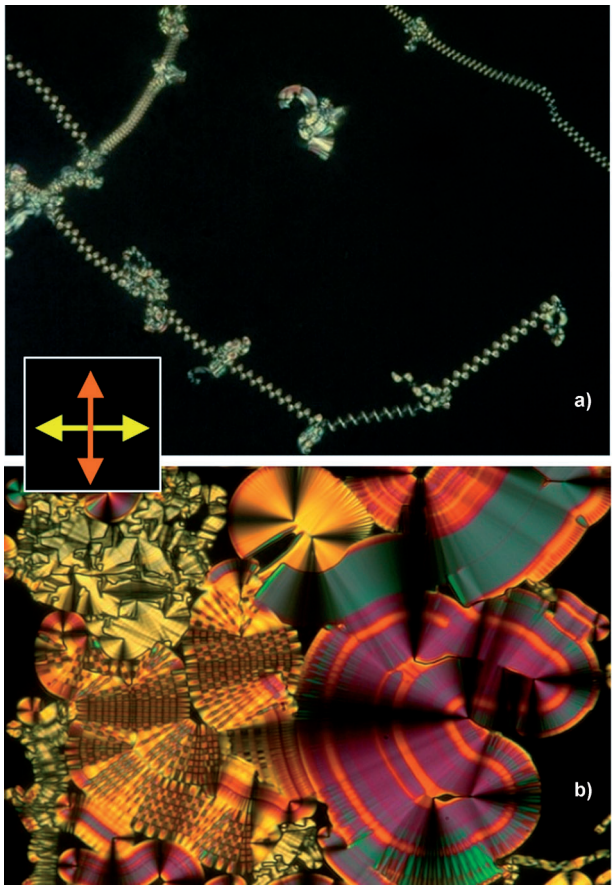

Figure 4. Different types of domains observed for PSM phase of **34-*14*OH**: a) Microfilaments of **34-*14*OH** at $T = 109\,°C$; b) Conformal domain texture of **34-*14*OH** at $T = 109\,°C$, with regions of checkerboard texture. These conformal domains originate from flattened microfilaments that fold and nest. The vertical size of the images (a) and (b) are 600 and 240 μm respectively.

perpendicular to the polarizer. Good contrast and visible edge definition at the boundaries can be realized. With time the birefringence does not change much but, in some focal conic domains, stripes appear at the edges. The other principal characteristic textural features observed for the **34-*n*OH** series of compounds are shown in Figure 5.

2.2. Photophysics and Photophysical Properties in Solutions

The incorporation of emission properties into organic LCs was always an active area of research. Emissive LCs is an intriguing system for materials research because they couple molecular self-assembly with intrinsic light generation capabilities. The absorption and emission spectra of all the compounds in the homologous series in dichloromethane solution are nearly superimposable and not much variation in the absorption maxima was observed with the chain length. The UV absorption and fluorescence spectroscopic properties of the representative compound **34-*14*OH** in solution were studied in various solvents of different concentrations to obtain the information regarding absorption and emission maxima, and the Stokes shift of fluorescence. The compound exhibited UV absorptions with an absorption peak at $\lambda = 349$ nm (3.55 eV, $\varepsilon \approx 62\,000\ L mol^{-1} cm^{-1}$). This absorption band, having a large molar absorption coefficient, reflects the π-π* transition of the π-conjugated system with a substituted phenyl benzoate unit as the core. Further, we investigated the fluorescence spectrum to observe the excited state characteristic features of the newly designed liquid crystalline materials. These compounds were examined in chloroform for their fluorescence in solution (λ_{em}) and it was found that the compounds exhibited strong fluorescence on excitation at $\lambda = 350$ nm (conc. 4.66×10^{-6} M).

The emission peak at $\lambda = 515$ nm (2.40 eV) with a large Stokes shift of the order of 165 nm (1.15 eV) was attributed to the formation of intermolecular excimer. The Stokes shift, which reflects the structural relaxation of the excited molecule and is significantly larger than the reported push-pull systems exhibiting LC behavior,[30–34] confirmed the molecular conformational changes upon excitation. The plot of the fluorescence spectra at different concentrations shows that the relative intensity of the peak at $\lambda = 515$ nm diminishes gradually with dilution, indicating the tendency of these molecules to form excimers in concentrated solution (Figure 6). These results are similar to those reported for molecular *J*-aggregates in which the excitonic energy is delocalized as a result of intermolecular coupling within the head-to-tail arrangement of the molecules in the solution.[35] The compounds exhibit fluorescence in the solid state also. The optical band gaps E_g of both compounds were determined from their absorption in thin solid film following the method of reference.[36] The E_g value obtained from UV spectrum is 3.26 eV.

2.3. FCPM and DTOM Studies

The spatial distribution of orientational order is an important feature of numerous soft matter systems of physical and chemical significance, including LC phases, each of which gives distinctive textures of molecular orientation. Of these, the structures and defects observed in banana LC phases, and, in particular, the PSM (B7), are unique and exotic. Here we report a study of the B7 textures using polarized fluorescence confocal imaging combined with DTOM. DTOM, for the LC between glass plates, integrates the 3D pattern of optical birefringence over the path of the light to give a 2D projection of the LC orientational structure. This limited ability to investigate the 3D structure is the principal motivation for additionally employing FCPM. To fully probe optic axis orientations within the focal conic domain, confocal FCPM imaging was performed here with different polarization states of the incident laser beam and fluorescent emission or depolarized transmission analyzer. These were controlled by using the polarization rotator in the FCPM setup (Figure 2).

Figure 7 shows the visualization of a circular focal conic domain of **34-*14*OH** (also known as toric focal conic domain) in its central region. The isotropic region away from the domain has uniform polarization-independent intensity. This is intermediate between the brightest within the domain, where the domain boundary is normal to the incident polarization, and the darkest, where the domain boundary is parallel to the polarization. The plot shows the fluorescence intensity $I(\theta)$,

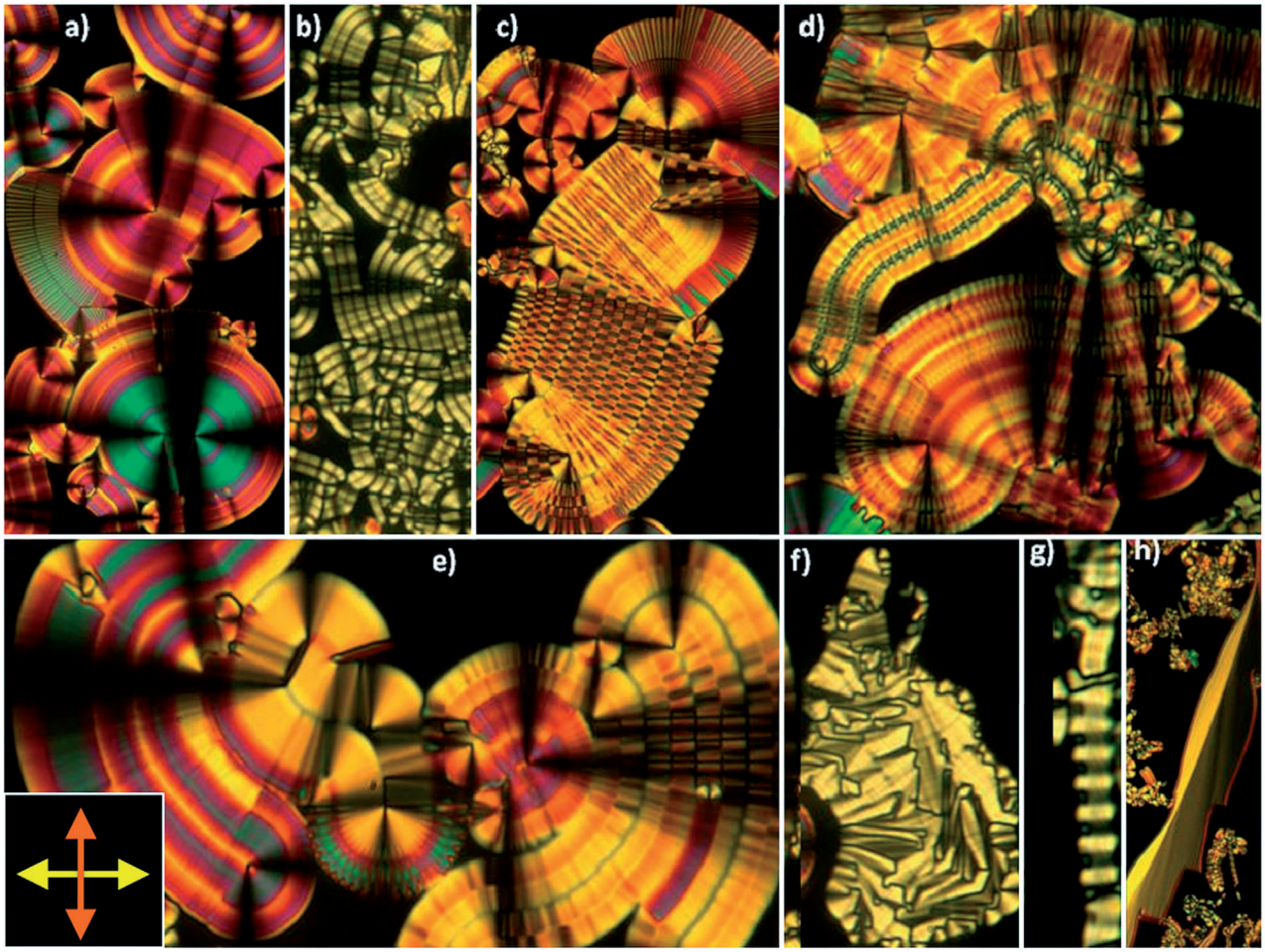

Figure 5. Typical textures observed in PSM phase of **34-*14*OH**: a) circular, b) surface trapped filament folding on the surface as it grows to form a 2D FCD, c) conformal domain with banded filaments, d,e) conformal domains with varying degrees of modulation, f,g) low birefringence 2D focal conic domain, and h) banana leaf-like domain.

measured along the inner circle (marked on the Figure 7 a) versus the azimuthal angle θ. These data can be well fit to the function in Equation (1):

$$T_{FCPM}(\theta) = A\cos^4\theta + B \quad (1)$$

This function is expected for a local orientation of fluorescence dipole along the layer normal, added to the background intensity B. A local distribution of image plane orientations, such as the one that would have anticlinic alternations in the upper half of Figure 7 b, with molecules tilted relative to the layer normal, would tend to round up the $\cos\theta^4$ minima of $I(\theta)$. However, for tilts less than approximately $\theta = 30^\circ$, such changes are not detectable in the current experiments, making tilt distribution information not accessible by FCPM. For the same domain DTOM produces an intensity according to Equation (2):

$$T_{DTOM}(\theta) = A\cos^2 2\theta + B \quad (2)$$

in which the period is $P\theta_{DTOM} = \pi/2$ in θ, compared to $T_{FCPM}(\theta)$, which has a period $P\theta_{FCPM} = \pi$, enabling FCPM to probe director orientation. Figure 6 thus shows that the molecular long

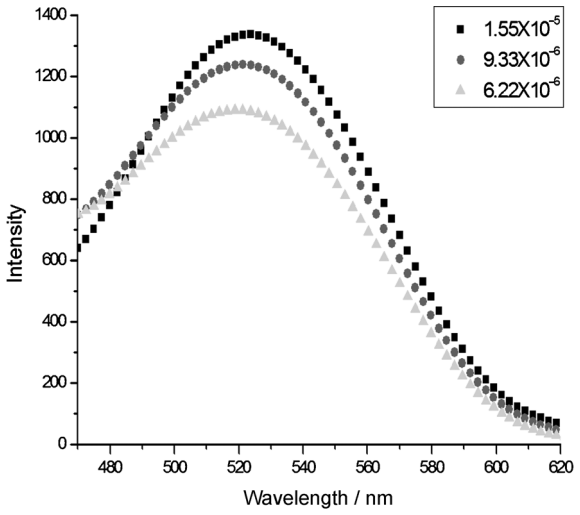

Figure 6. Concentration dependent fluorescence spectra of **34-*14*OH** on excitation at $\lambda = 350$ nm in $CHCl_3$

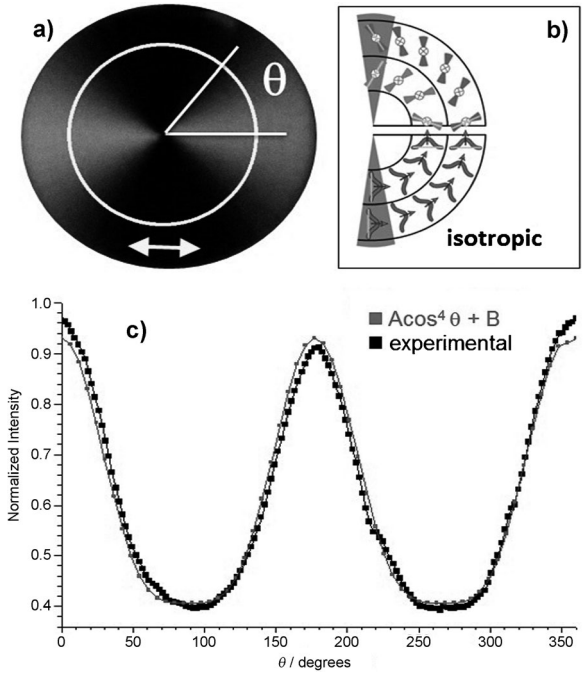

Figure 7. An FCPM image a) of a circular focal conic domain obtained with the linear polarization of the laser excitation and detected fluorescence light along the horizontal direction marked by the double arrow. The domain is schematically shown in (b). The intensity versus angle shown in (c) was measured along the line marked in (a). A and B are the fitting parameters used to fit the experimental data points by the anticipated angular dependence of the FCPM intensity.[21]

axis orientation is on average radial in this domain, indicating that the layers are circular, that is, tangent to the domain boundary. The fluorescence intensity is also affected by the thickness of the domain, which, in the case of the B7 domains, may be less than the cell gap. On the other hand, the isotropic phase can be assumed to fill the gap, its fluorescence yield corresponding to a random distribution having the cell thickness. Thus, B7 regions having orientation in the image plane with layer normal parallel to the polarization domains and filling the cell gap should be brightest in the FCPM textures, as observed in our experiments.

The DTOM textures of **34-*14*OH**, obtained with crossed polarizer and analyzer using either white light or monochromatic light of $\lambda = 488$ nm, presented in Figures 4, 5, and 8 g,h show a variety of coexisting structures distinctive of the B7. These include: 1) birefringent helical microfilaments (Figure 4 a), typically the first things to appear upon cooling from the isotropic; 2) conformal domains having birefringence that is large, that is, comparable to the cylindrical, locally bookshelf domains of the bent-core B2 phases, but highly variable, generating a host of different birefringence colors (Figures 4, 5, and 8 g,h); 3) conformal domains of low birefringence (Figures 5 f,g and 8 g,h); 4) patterns of birefringence including checkerboards (Figures 4 b, 5 c, and 8 g) and stripes (Figures 4, 5, and 8 g,h); and 5) the isotropic regions, black between crossed polarizer and analyzer in DTOM (Figures 4, 5, and 8 g,h). Figure 8 shows the same textural area imaged in both the FCPM (a–f) and DTOM (g, h) modes. The FCPM images obtained for two orthogonal

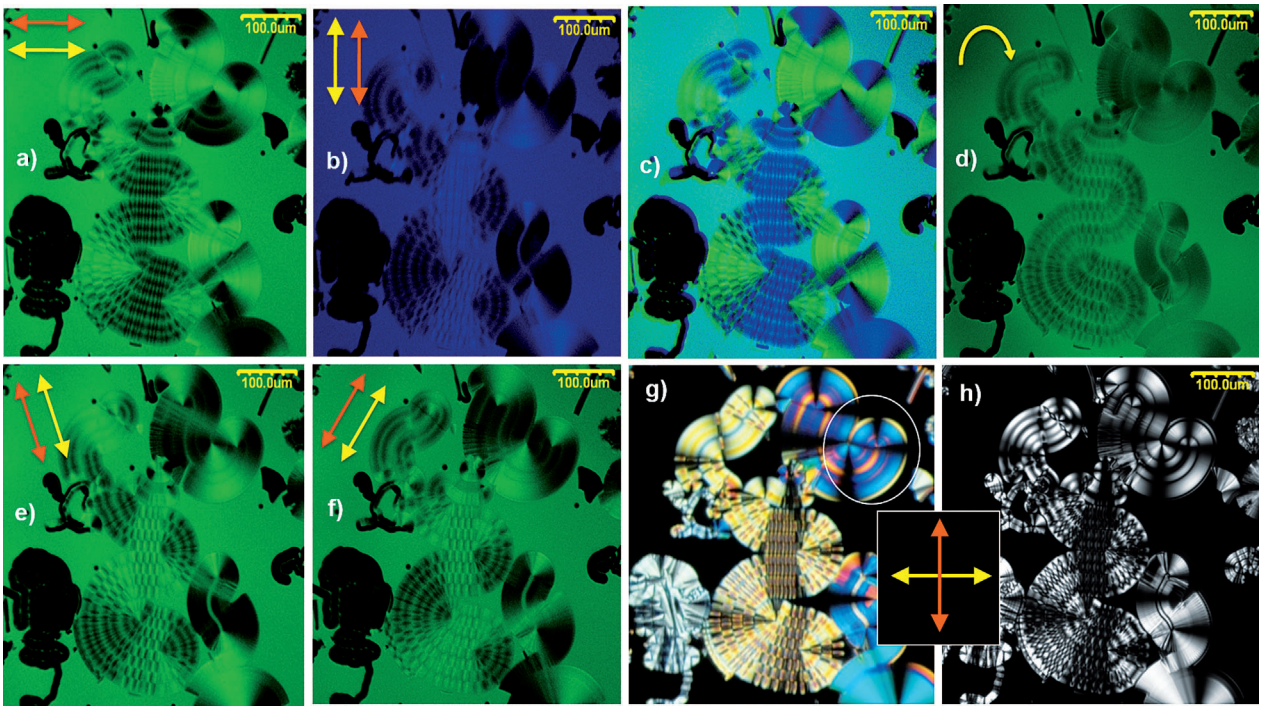

Figure 8. FCPM (a–f) and depolarized transmission optical microscopy (DTOM) (g,h) images of **34-*14*OH** with different states of excitation polarization (a,b,d,e,f, and horizontal arrow for g,h) and analyzer polarization (a,b,d,f, and vertical arrow for g,h): a) with horizontal polarization; b) with vertical polarization; c) overlay image of (a) and (b); d) corresponding confocal image with circular incident polarization; e,f) oblique polarization $\theta = 45^\circ$ clockwise and anticlockwise as indicated, obtained rotating the polarization state with a polarization rotator; and g,h) DTOM images with white and monochromatic light respectively. FCPM images are of a ($\approx$10 μm thick) slice parallel to the cell plates through the cell center (see Figure 9).

linear polarizations and their overlay image are shown in Figure 8 a–c, in which the image with horizontal polarizer and analyzer is shown in the darker regions and the image with vertical polarizer and analyzer shown in lighter regions.

Examples of information available in the FCPM images can be understood with the help of Figure 9, which shows a B7 stripe domain, imaged in DTOM with monochromatic (d) and white (e) light, and in FCPM showing *XY* (a–c,f) and *XZ* (g) 3D structural cross sections of fluorescence emission and thus orientational structure. The FCPM images are obtained using excitation light polarized and fluorescence light analyzed in Figure 9. In Figure 9 (a) this is along the y direction (horizontal on the page), and in (c) with light polarized and analyzed along the x direction. This is shown in an *XY* cross-section along the cell center plane in z, normal to the glass plates, along the second line from the top in Figure 9 (g), and an *XZ* cross-section of the plane indicated by the red line in (f).

The isotropic regions again show up as the domains of uniform intermediate intensity, as expected for a random distribution of orientations. From Figure 7, which is a slice through the cell center parallel to the *XY* plane, the brushes are of the highest intensity if the molecular long axis is parallel to the optical polarization. Figure 9 shows that, as in Figure 7, the molecules in the domains are normal to the domain boundaries with the isotropic regions, and thus the smectic layers are parallel to these boundaries, as in Figure 7. Therefore they are also parallel to the stripes of intermediate intensity that modulate the domains. As in Figure 7, orientations with the optic axis locally parallel to the polarization are substantially brighter than the isotropic. Figure 9 a,f illustrate that where the stripes and isotropic boundaries turn to be parallel to the polarization the fluorescence intensity becomes quite low, such that regions where the layer normal is rotated to more than approximately $\theta = 60^{\circ}$ from the polarization will have the lowest (black) green level. Notably in Figure 9 a,f is that the stripes separating bright regions within the domains have the same hue as the isotropic domains no matter how they are oriented in the *XY* plane This indicates that they are, in fact, isotropic walls separating birefringent 20-micron scale filaments with the smectic layers running parallel to their lengths. The *XZ* cross-section shows that these stripes and their isotropic spacers pass entirely through the sample, in agreement with this picture. A remarkably consistent feature of B7 textures of a particular highly repetitive structure within a domain, but entirely different from that of other domains (see Figure 5 c for example). The observations of Figure 9 a,f suggest strongly that these domains are generated by single microfilaments, approximately 20 μm in scale, that are homogeneous along their length and flexible, and folded back and forth upon themselves with a fixed gap of isotropic material in between to make a 3D structure. The sketch shows the *XZ* cross-section of the smectic layers suggested by the FCPM imaging. The monochromatic DTOM image gives a good indication of the precision of the translational symmetry along the microfilament that flattens and folds to make the domain.

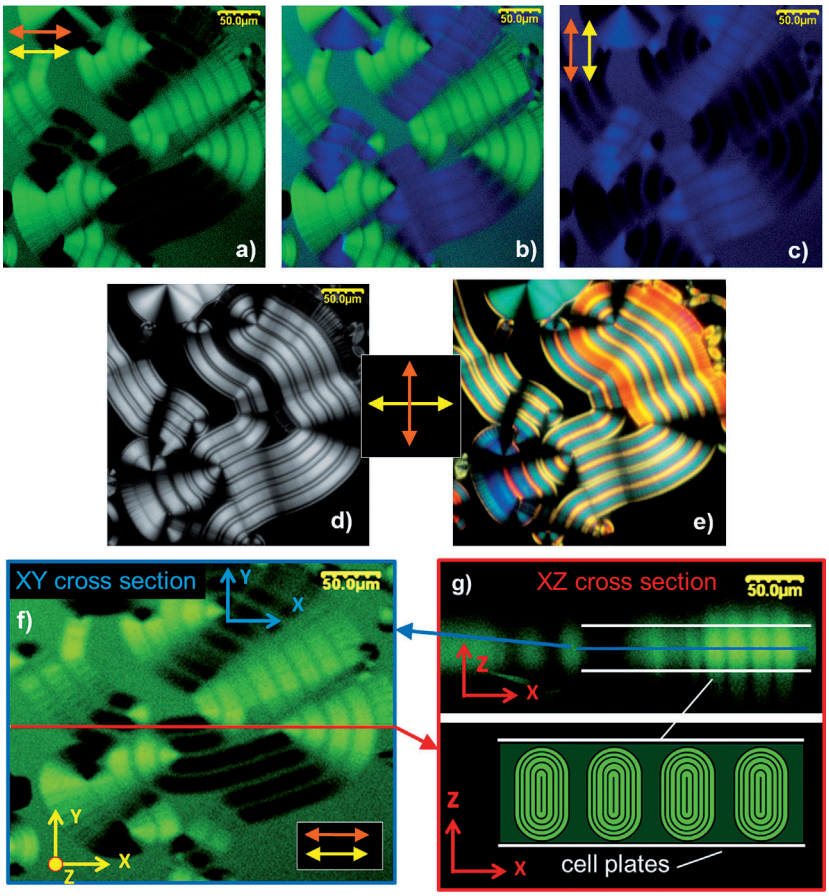

Figure 9. FCPM images (a–c) of **34-*14*OH** with a) horizontal polarization; c) vertical polarization; and b) overlay image of (a) and (c). DTOM images (d,e) with monochromatic (d) and white (e) light respectively. FCPM images (f,g) showing in f) an *XY* cross-section of the circular focal conic domain, in the cell center along the second line from the top in (g), and in g) the *XZ* cross-section along the horizontal line in the center of (f). The other horizontal lines indicate the LC/glass boundaries in the cell along z.

Comparison of the white light image in Figure 9 e with the FCPM image in Figure 9 a shows correlated variation of FCPM intensity and white light birefringence color, with regions of lower birefringence phase shift corresponding to the darker stripes in FCPM.

Figures 10 and 11 show conformal domains probed by the FCPM and DTOM imaging, which enables, along with Figure 8, a comparison of these imaging modes to be made. The white-light DTOM images show that the highest birefringence do-

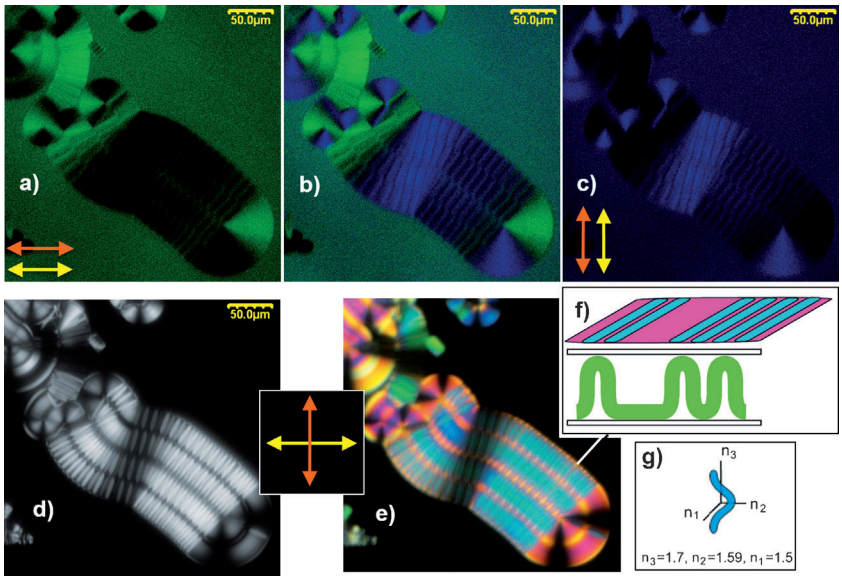

Figure 10. FCPM (a–c) and DTOM (d,e) images of a banded conformal PSM domain of **34-*14*OH**. The banding is due to undulation of the flattened microfilament across the cell as indicated in (f); g) typical bent core molecule refractive indices. The birefringence colors indicate that the flattened microfilaments do not fill the cell gap.

mains, those that fill the largest fraction of the cell gap, exhibit Michel–Levy colors in the second-order band, with birefringent path differences Δnd in the range $600\ \text{nm} < \Delta nd < 1100\ \text{nm}$. Such domains are seen in Figures 8g, 10, and 11. The Δnd of the domain in the white circle in Figure 8g varies from Δnd of approximately 970 nm to Δnd of approximately 1170 nm. With typical bent-core material's refractive indices, indicated in Figure 10g,[37] giving an average Δn of approximately 0.12, these Δnd values indicate that many of the B7 conformal domains do not completely fill the cell gap. The bands in the circled domains are visible in the FCPM images as stripes of intermediate intensity, darker than the brightest orientations and brighter than the darkest, indicating that they are more orientationally disordered than the regions in which Δnd is 1170 nm and not just thinner.

It is also noticeable in Figure 8 that in the higher birefringence domains the corresponding bright orientations in the FCPM images are significantly brighter than the surrounding isotropic, whereas in the lower birefringence domains they are comparable or less bright. In particular Figures 4b, 5g,h, 8, and 12 show several distinctly thinner domains, with Michel–Levy colors in the lower range of the first order band with $\Delta nd < 400$ nm, these show up as very dark or black in the FCPM imaging. These domains have image plane stripes that are much larger in width than their thickness and thus a structure of flattened race track-shaped filaments that are thinner than their width, as sketched in Figure 12d. The layer normal and mean molecular long axis produce little fluorescence intensity because they are largely normal to the cell plates in such domains. This is because the viewing direction is nearly along the emission dipole axis, but the inlayer plane polar order and consequent biaxiality produces weakly birefringent textures. Images in Figure 12e,g of such a domain for the two orientations of polarizer and analyzer shows that they are dark in FCPM for either orientation of linear polarization of excitation light.

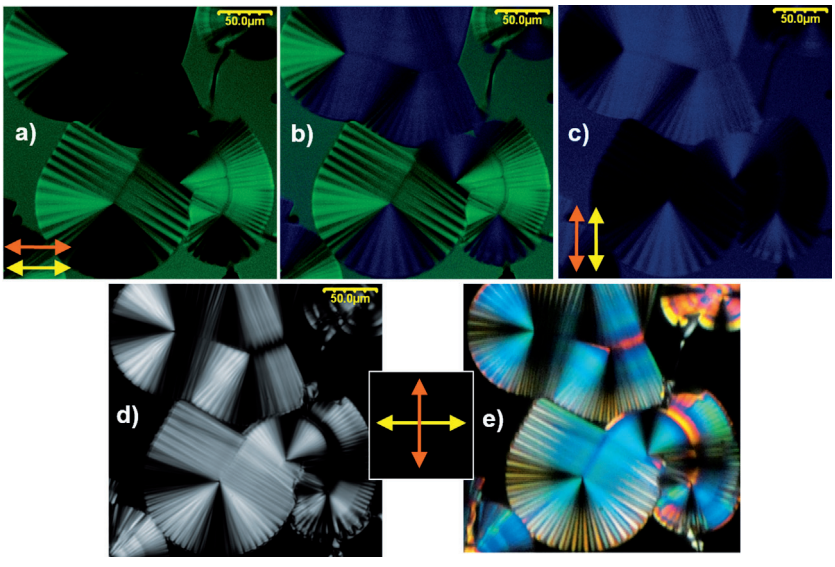

Figure 11. FCPM (a–c) and DTOM (d,e) images of a banded conformal PSM domain of **34-*14*OH**. The birefringence colors indicate that the flattened microfilaments do not fill the cell gap.

The domain of Figure 10 results from the folding of a filament, but with the variation that the texture is modulated along the filament direction to make the filaments appear banded, with the bands running normal to the filament long axis. These bands appear in the center where the filament segments are nearly straight, but not at the ends where the filament segments are bent into circles. Figure 8 shows a similar banded domain but with the banding on both the curved and straight portions of the filament. The FCPM images in Figure 8 show that there is a significant ($\theta \approx 10$–15°) modulation in azimuthal molecular orientation in the plane of the image associated

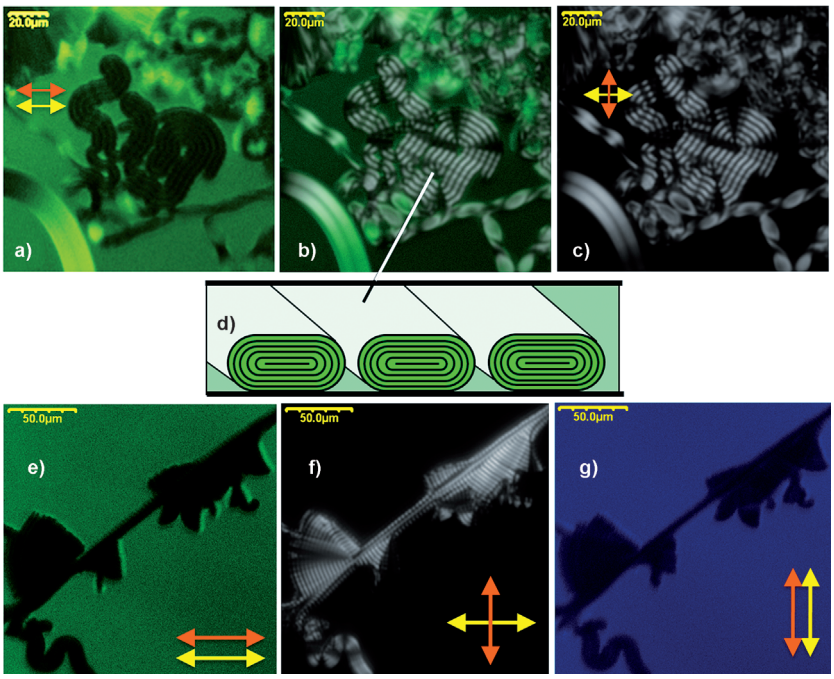

Figure 12. FCPM (a) and DTOM (c), and overlap (b) images of principally homeotropic domains of **34-*14*OH**. These domains are from filaments that are much thinner than they are wide and do not fill the cell gap, as sketched in (d). Incident polarization is substantially in the layer plane and therefore substantially normal to the molecular long axes resulting in weak fluorescence excitation and thus the dark appearance of these domains. FCPM (e,g) and DTOM (f) image (e) of a weakly birefringent domain.

with the banding, whereas this modulation is much smaller in Figure 10 ($\theta \approx 3$–5°). The birefringence images show that the banding increases the birefringence, the color changing from pink to cyan in Figure 10e and from whitish yellow to pink in Figure 8g. The increase in birefringence indicates an effective thickening of the domain in the bands, which is most readily achieved by tilting the microfilaments locally about an axis parallel to the cell plates and normal to the filament axis. In the banding such tilt is a periodic modulation yielding a microfilament that undulates back and forth toward alternate cell plates, as sketched in Figure 10f. The images in Figure 8 show dramatically that the in-plane azimuthal modulation in adjacent stripes is mutually $\theta = 180^\circ$ out of phase, leading to the checkerboard pattern in the places where the polarization is oblique to the domain stripe axis. The domain of Figure 10 exhibits a less obvious but similar organization. This sort of phase coherence indicates that the azimuthal orientation in a stripe is coupled at the stripe–stripe interface to that in the neighboring stripe.

A distinctly different characteristic B7 texture feature is the "banana leaf" domain, examples of which are shown in Figures 5h and 13 and imaged in FCPM and DTOM in Figure 13. These domains appear quite dark in FCPM images if oriented with their long direction normal to the linear polarization direction of excitation light, as in Figure 13a, but quite bright for polarization normal to their long axes. This indicates that the layer normal is also in this direction, with the layers also normal to the cell plates as indicated in the schematic in Figure 13c. These orientations are in agreement with structural analysis based on XRD, optical rotation, and birefringence measurements reported previously.[9] The weakly birefringence of these domains indicates third order birefringence, and thus that they fill the entire cell gap.

Upon cooling the isotropic phase toward the transition to the B7, the B7 first appears in the form of helical B7 microfilaments that grow in great number and variety into the isotropic (see Figure 4a for a DTOM image).[3] Figures 14 and 15 show corresponding FCPM and DTOM images of several common microfilament morphologies. The FCPM intensity difference on the two arms of a filament with a $\theta = 90^\circ$ bend in Figure 14a–c shows that the orientation of the molecules is generally normal to the microfilaments. This indicates that the layers are generally parallel to the microfilament axis, similar to the freely suspended macrofilaments that can be pulled in air.[9] Unlike the macrofilaments in air, which if freshly pulled have the modulation wave vector normal to the filament axis, structuring the layers similar to fluted Greek columns,[9] the microfilaments grow into the

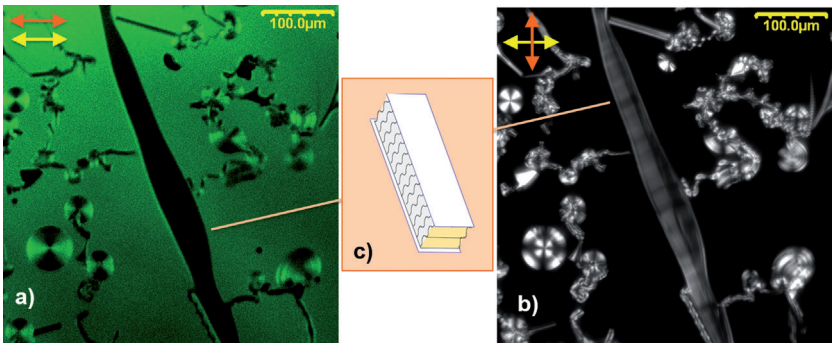

Figure 13. FCPM (a) and DTOM (b) images of a banana leaf domain of **34-*14*OH**, in which the layers are uniformly oriented normal to the cell plates and to the long axis of the domain. The splay modulation wave vector is normal to the cell plates, leading to layer undulations as sketched in (c).

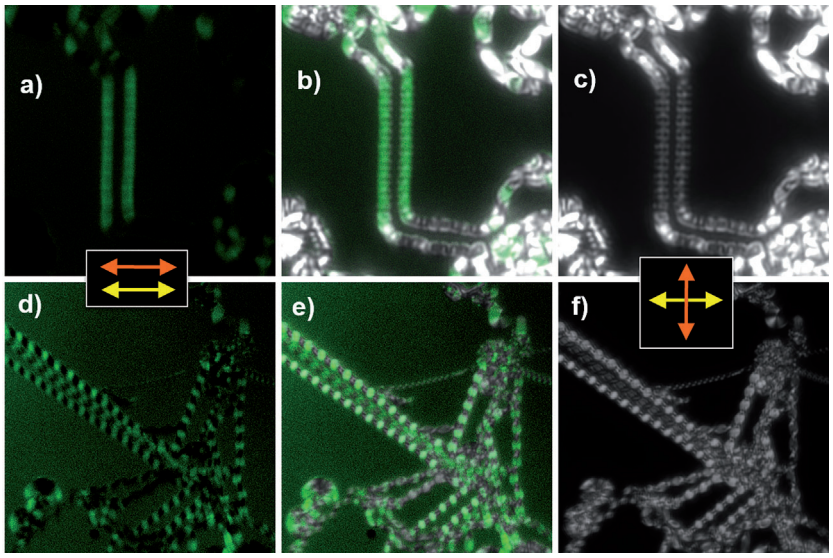

Figure 14. FCPM (a,d) and DTOM (c,f), and overlap (b,e) images of helical PSM phase filaments growing in **34-*14*OH** cooled from the isotropic. In this orientation the domain is dark in FCPM because the excitation polarization is substantially normal to the molecular long axes. The fluorescence intensity of the $\theta = 90^{\circ}$ bent filament of (a–c) shows that the smectic layers run parallel to the filament axis.

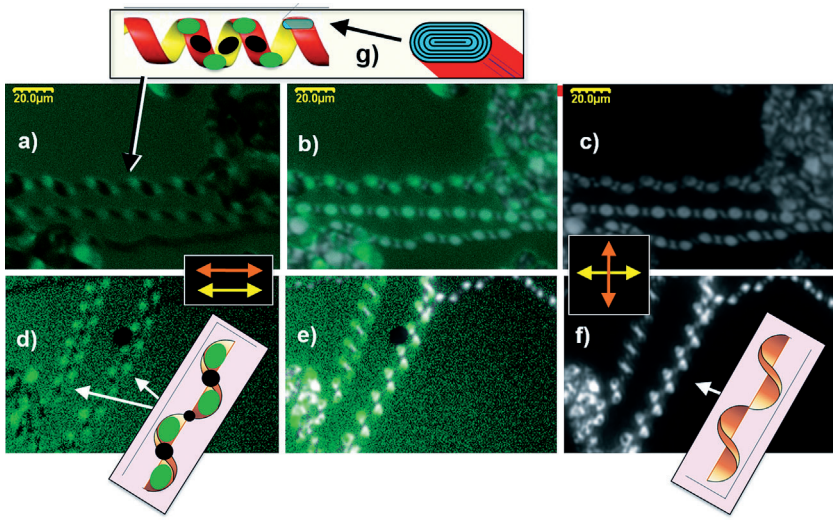

Figure 15. FCPM (a,d) and DTOM (c,f), and overlap (b,e) images of helical PSM phase filaments growing in **34-*14*OH** cooled from the isotropic. Filaments are flattened ribbons which can helically wind in either a phone cord motif (a–c), or a screw auger motif (d–f). Dark spots along the filaments in the FCPM images arise either from homeotropically oriented filament segments (a–c,g), or from excitation normal to the molecular long axes (d–f).

isotropic domains with a variety of helical windings of the modulation about the filament axis. This produces a macroscopic helical distortion of the filaments. This distortion, once commenced in a particular fashion, is rigorously maintained as the filament grows in length. Nine such helically wound filaments show distinctive alternating bright and dark patterns in the FCPM and DTOM modes in Figures 14d–f and 15. That the optical period in θ for DTOM intensity versus θ is twice that for FCPM intensity versus θ is particularly clear in the images of Figures 14d–f and 15a–c. The local cross-sections helically wound microfilaments are generally race-track shaped. Figure 15 showing the microfilament structures emerging from the two extreme limits of race track orientation, either extended parallel to the filament axis, giving a phone cord-type geometry (a–c), or extended normal to the filament axis, giving a screw auger-type geometry (d–f). In the phone cord case the dark spots along the FCPM filament image occur where the flat sides of the microfilament are normal to the viewing direction, minimizing the fluorescence intensity as in the case of the dark domains of Figures 8 and 12. In the auger case the dark spots are the places along the helix where the layer planes are parallel to the excitation and emission polarizations, with those on the front side showing a different intensity from those on the back side in both filaments.

Figure 16 shows an isolated microfilament with an approximately circular cross-section exhibiting a folding that is generally loose except for in a few places in which adjacent parts of the filament run parallel. The filling of the gaps with the isotropic phase is clear in this case. Also evident in the FCPM image are the brightest regions in which the filament axis is locally vertical. The high fluorescence intensity indicates that in these regions the orientation of the molecular long axes is locally normal to the filament axis, indicating that the filament structure is locally a set of nested cylindrical smectic layers. Overall however the filament structure is much more complex and it can be seen that there are several areas where the filament is locally vertical but not bright. The bright vertical regions appear in the DTOM image of Figure 16b as roughly 3/4 of a circular focal conic domain with smooth dark brushes. The less bright vertical regions appear to have sharp dark lines across the filament in the DTOM image, suggestive of some kind domain boundary.

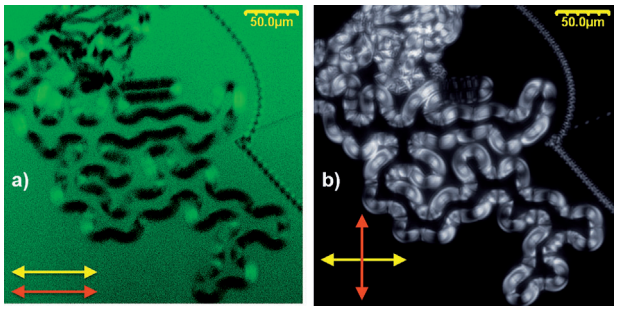

Figure 16. FCPM (a) and DTOM (b) images of an isolated microfilament domain of **34-*14*OH** in which the circular cross-section filament exhibits a loose folding.

2.4. B7 Textures

FCPM has enabled the first visualization of the textures of the B7 phase in three dimensions, from which several definitive conclusions can be drawn: 1) the FCPM observations confirm the basic structural motif of the conformal domain textures outlined in Figure 1b,c, namely the bending and packing of translationally symmetric filaments have, in general, race track-shaped sets of nested smectic layers as cross sections. The often rigorously enforced translational invariance along the filament, apparent in Figures 8g, 9, 10, 15, and 16, for example, is evidence for the maintenance of the filament profile by the combination of smectic layering and undulation periodicities. The in-plane folding of the filaments is a consequence of the injection of molecules all along the filaments during the cooling process, increasing their length at a fixed cross-section. 2) The textures also exhibit a variety of situations in which the translational symmetry along the filament is broken, in particular by periodic modulations of various sorts. Generally, the current implementation of FCPM does not have spatial resolution to characterize these uniquely. 3) Application of FCPM to the structure of isolated helical filaments, as in Figures 15 and 16, is a uniquely powerful probe of their structure.

3. Conclusions

We have demonstrated that fluorescence confocal polarized microscopy offers new opportunities for understanding the structures and textures of LCs. We applied it here to the PSM (B7) phases, a study made particularly effective by the use of a novel, strongly fluorescent bent-core compound **34-*14*OH** that exhibits the B7 phase. These results highlight the **34-*n*OH**s as a promising family of materials for use as fluorescent probes in bent-core systems, owing to their efficient fluorescence emission and possibilities for permutation and combinations of elements of their molecular architecture. The efficiency of the emitted light can be readily tuned in these systems by chemical grafting with opportune central cores. In addition to the FCPM studies of pure B7 liquid crystal systems, the three-dimensional imaging capability that we demonstrate can be extended to the study of director structures in LC-colloidal composites[38] and to multi-photon orientation-sensitive imaging techniques such as two-photon and three-photon excitation fluorescence polarizing microscopy.[39]

Acknowledgements

We acknowledge discussions with Rahul K. Nath, Qingkun Liu and Rahul Trivedi and technical assistance of Chris Twombly, Dennis Gardner and Clayton Lapointe. This work was supported by the US National Science Foundation MRSEC Grants DMR-0820579 and DMR-1420736.

Keywords: fluorescence · liquid crystals · photophysical · splay modulated · textural analysis

[1] G. Pelzl, S. Diele, A. Jakli, Ch. Lischka, I. Wirth, W. Weissflog, *Liq. Cryst.* **1999**, *26*, 135 – 139.
[2] J. P. Bedel, J. C. Rouillon, J. P. Marcerou, M. Laguerre, H. T. Nguyen, M. F. Achard, *J. Mater. Chem.* **2002**, *12*, 2214 – 2220.
[3] A. Jakli, Ch. Lischka, W. Weissflog, G. Pelzl, A. Saupe, *Liq. Cryst.* **2000**, *27*, 1405 – 1409.
[4] C. K. Lee, A. Primak, A. Jakli, E. J. Choi, W. C. Zin, L. C. Chien, *Liq. Cryst.* **2001**, *28*, 1293 – 1299.
[5] R. A. Reddy, B. K. Sadashiva, *Liq. Cryst.* **2003**, *30*, 273 – 283.
[6] H. N. S. Murthy, B. K. Sadashiva, *Liq. Cryst.* **2003**, *30*, 1051 – 1055.
[7] G. Heppke, D. D. Parghi, H. Sawade, *Liq. Cryst.* **2000**, *27*, 313 – 320.
[8] S. Umadevi, A. Jakli, B. K. Sadashiva, *Soft Matter* **2006**, *2*, 215 – 222.
[9] D. A. Coleman, J. Fernsler, N. Chattham, M. Nakata, Y. Takanishi, E. Korblova, D. R. Link, R. F. Shao, W. G. Jang, J. E. Maclennan, O. Mondainn-Monval, C. Boyer, W. Weissflog, G. Pelzl, L. C. Chien, J. Zasadzinski, J. Watanabe, D. M. Walba, H. Takezoe, N. A. Clark, *Science* **2003**, *301*, 1204 – 1211.
[10] G. Pelzl, S. Diele, W. Weissflog, *Adv. Mater.* **1999**, *11*, 707 – 724.
[11] H. Takezoe, Y. Takanishi, *Jpn. J. Appl. Phys.* **2006**, *45*, 597 – 625.
[12] R. A. Reddy, C. Tschierske, *J. Mater. Chem.* **2006**, *16*, 907 – 961.
[13] R. Deb, R. K. Nath, M. K. Paul, N. V. S. Rao, F. Tuluri, Y. Shen, R. Shao, D. Chen, C. Zhu, I. I. Smalyukh, N. A. Clark, *J. Mater. Chem.* **2010**, *20*, 7332 – 7336.
[14] T. Niori, T. Sekine, J. Watanabe, T. Furukawa, H. Takezoe, *J. Mater. Chem.* **1996**, *6*, 1231 – 1233.
[15] D. R. Link, G. Natale, R. Shao, J. E. Maclennan, N. A. Clark, E. Korblova, D. M. Walba, *Science* **1997**, *278*, 1924 – 1927.
[16] R. A. Reddy, B. K. Sadashiva, R. A. Raghunathan, *Chem. Mater.* **2004**, *16*, 4050 – 4062.
[17] B. Das, S. Grande, W. Weissflog, A. Eremin, M. W. Schroder, G. Pelzl, S. Diele, H. Kresse, *Liq. Cryst.* **2003**, *30*, 529 – 539.
[18] T. J. Dingemans, N. S. Murthy, E. T. Samulski, *J. Phys. Chem. B* **2001**, *105*, 8845 – 8860.
[19] K. M. Fergusson, M. Hard, *J. Mater. Chem.* **2010**, *20*, 3069 – 3078.
[20] D. Ki Yoon, R. Deb, D. Chen, E. Körblova, R. Shao, K. Ishikawa, N. V. S. Rao, D. M. Walba, I. I. Smalyukh, N. A. Clark, *Proc. Natl. Acad. Sci. USA* **2010**, *107*, 21311 – 21315.
[21] I. I. Smalyukh, S. V. Shiyanovskii, O. D. Lavrentovich, *Chem. Phys. Lett.* **2001**, *336*, 88 – 96.
[22] I. I. Smalyukh, R. Pratibha, N. V. Madhusudana, O. D. Lavrentovich, *Eur. Phys. J. E* **2005**, *16*, 179 – 191.
[23] Q. Liu, C. Beier, J. Evans, T. Lee, S. He, I. I. Smalyukh, *Langmuir* **2011**, *27*, 7446 – 7452.
[24] T. Lee, R. P. Trivedi, I. I. Smalyukh, *Opt. Lett.* **2010**, *35*, 3447 – 3449.
[25] R. P. Trivedi, I. I. Klevets, B. Senyuk, T. Lee, I. I. Smalyukh, *Proc. Natl. Acad. Sci. USA* **2012**, *109*, 4744 – 4749.
[26] T. Lee, B. Senyuk, R. P. Trivedi, I. I. Smalyukh, *Soft Matter*, in press, **2013**.
[27] A. C. Sentman, D. L. Gin, *Adv. Mater.* **2001**, *13*, 1398 – 1401.
[28] S. Benning, H. S. Kitserow, H. Bock, M. F. Achard, *Liq. Cryst.* **2000**, *27*, 901 – 906.
[29] T. Christ, B. Glusen, A. Greiner, A. Kettner, R. Sander, V. Stumpflen, V. Tsukruk, J. H. Wendorff, *Adv. Mater.* **1997**, *9*, 48 – 52.

[30] H. Gallardo, R. Cristiano, A. A. Vieira, R. A. W. N. Filho, R. M. Srivastava, I. H. Bechtold, *Liq. Cryst.* **2008**, *35*, 857 – 863.
[31] A. A. Vieira, R. Cristiano, A. J. Bortoluzzi, H. Gallardo, *J. Mol. Struct.* **2008**, *875*, 364 – 371.
[32] R. M. Srivastava, R. A. W. N. Filho, R. Schneider, A. A. Vieira, H. Gallardo, *Liq. Cryst.* **2008**, *35*, 737 – 742.
[33] R. Cristiano, F. Ely, H. Gallardo, *Liq. Cryst.* **2005**, *32*, 15 – 25.
[34] A. A. Vieira, R. Cristiano, F. Ely, H. Gallardo, *Liq. Cryst.* **2006**, *33*, 381 – 390.
[35] F. Camerel, L. Bonardi, M. Schmutz, R. Ziessel, *J. Am. Chem. Soc.* **2006**, *128*, 4548 – 4549.
[36] A. Joshi, M. O. Manasreh, E. A. Davis, B. D. Weaver, *Appl. Phys. Lett.* **2006**, *89*, 111907.
[37] M. Nakata, D. Chen, R. Shao, E. Körblova, J. E. Maclennan, D. M. Walba, N. A. Clark, *Phys. Rev. E* **2012**, *85*, 031704.
[38] B. Senyuk, Q. Liu, S. He, R. D. Kamien, R. B. Kusner, T. C. Lubensky, I. I. Smalyukh, *Nature* **2013**, *493*, 200 – 205.
[39] R. Herges, *Chem. Rev.* **2006**, *106*, 4820 – 4842.

Received: June 7, 2014
Published online on September 26, 2014